SrCuP and SrCuSb Zintl phases as potential thermoelectric materials

A. Moll, A. Hamidou, J.-C. Crivello, J.-M. Joubert, E. Alleno, C. Barreteau

SrCuP and SrCuSb Zintl phases as potential thermoelectric materials

A. Moll [a,*], A. Hamidou [a], J.-C. Crivello [a], J.-M. Joubert [a], E. Alleno[a], C. Barreteau [a,*]

[a] Université Paris Est Créteil, CNRS, ICMPE, UMR7182, F-94320, Thiais, France

Abstract

We report the investigation of the thermoelectric properties of SrCu*X* (*X* = P or Sb), combining experiments and DFT calculations, for the first time for SrCuP. These two compounds were recently highlighted by our high-throughput calculation for screening new thermoelectric materials. These calculations showed that these compounds are stable and non-metallic, and so suitable for thermoelectric applications. They were synthesized in the present work and our experimental results confirm the non-metallic character of these two compounds, which is favorable for thermoelectricity. The crystal structure of the materials is depicted within the Zintl model, showing graphene-like Cu*X* layers promoting the electronic transport. High charge carriers mobilities ($\mu = 30$ cm^2 V^{-1}.s^{-1} in SrCuP, $\mu = 200$ cm^2 V^{-1}.s^{-1} in SrCuSb at room temperature) and low effective density of states masses ($m^* = 0.7\ m_e$ for SrCuP, $m^* = 0.4\ m_e$ for SrCuSb) were therefore determined. Moreover, despite a quite simple crystal structures, low lattice thermal conductivities were measured ($\lambda_{ph} < 3.3$ W.m^{-1}.K^{-1} for both compound), which is favorable to thermoelectricity. Explanations of this result are provided by first-principles calculation of the vibrational properties. Promising values of the thermoelectric figure of merit *ZT* = 0.20 (*X* = P) at 600 K and *ZT* = 0.14 (*X* = Sb) at 650 K were finally measured in the pristine compounds. These values could probably be improved by doping.

Keywords : Zintl phases, Mechanical alloying, Phosphorus-based materials, Thermoelectric, High mobility, low thermal conductivity,

1 Introduction

The demand of clean and renewable energy sources has increased over the last decades in response to economic and environmental concerns. Among technologies in development, the thermoelectricity enables the direct conversion of heat into electricity. The thermoelectric materials

*Corresponding authors:
adrien.moll@universite-paris-saclay.fr (Adrien Moll)
celine.barreteau@cnrs.fr (Céline Barreteau)

are small gap semiconductors with a conversion efficiency related to the dimensionless figure of merit, $ZT = S^2T/\rho\lambda$, with S, the Seebeck coefficient, ρ, the electrical resistivity, λ, the thermal conductivity and T, the temperature. Nowadays, the conventional thermoelectric materials used in commercial devices, such as Bi_2Te_3, Si-Ge or Pb-Te alloys, for example, have maximal ZT values around 1 at their respective operating temperature [1–4]. However, their use is limited by the toxicity, scarcity and/or the high cost of their constituents. There is an important need to develop of new stable, non-toxic, and low-cost thermoelectric materials.

We recently reported a method based on high-throughput calculations to screen new thermoelectric materials [5,6]. The thermodynamic stability and the electronic properties of thousands of ternary intermetallic compounds with equimolar *TMX* compositions were calculated with *T*, a transition metal from the Ti, V, Cr columns, Sr, Ba, Y and La, *M*, an element from the first row of transition metals and *X*, a *sp* element (Al, P, Si, Sn and Sb)). The objective was to discover new stable and non-metallic materials with promising properties for thermoelectricity.

Among the equimolar *TMX* materials, those crystallizing in the cubic MgAgAs structure-type ($F\bar{4}3m$), known as half-Heusler, exhibit interesting thermoelectric properties as in TiCoSb [7], TaCoSn [8], TiNiSn[9] or TaFeSb[10]. Recently, high-throughput calculations [6] as well as experimental investigations, have also shown that semiconducting compounds can also be found in the orthorhombic, TiNiSi structure type as in doped-TiNiSi [11].

Equimolar *TMX* combinations can also crystallize in other structure-type such as the hexagonal BeZrSi type ($P6_3/mmc$ (N° 194) space group). In our previous theoretical studies from 2019 [5,6], we have shown that several compounds with this structure are predicted as non-metallic. In 2020, the computational prediction made by Gorai *et al* [12] also reported *ABX* Zintl compounds as promising thermoelectric materials, with *A* from the alkali column and a similar hexagonal structure type. Recent experimental studies of the thermoelectric properties of BaAgAs [13], BaAgSb [14] and BaAgBi [15] confirmed these predictions. Due to their quasi-2D crystal structure made of covalent

[AgX]$^{2-}$ honeycomb plans (X=As, Sb or Bi) with rattling Ba^{2+} atoms, high charge carriers mobilities and low lattice thermal conductivities were measured, leading to a maximal ZT value of 1.3 obtained in $Ba_{1.01}AgSb$ at 1012 K, opening very interesting possibilities for thermoelectricity.

Among compounds with BeZrSi type structure, our theoretical studies [5,6] also highlighted SrCuP and SrCuSb as potential candidates for thermoelectricity. The use of Cu as transition metal instead of Ag is favorable for price reduction of the materials. The structural studies of SrCuP and SrCuSb were reported for the first time by Mewis in 1978 [16] and Eisenmann *et al.* in 1974 [17] respectively. The first experimental study of the properties of SrCuSb has been reported very recently in 2022 by Zheng *et al.* [18], confirming a remarkable high charge carrier mobility and low lattice thermal conductivity in this material leading to a ZT value of 0.30 at 1000 K. As for ternary copper-phosphide materials, the only measurements were made by Quinn *et al*. [19] in 2022 on MgCuP and CaCuP, measuring interesting *ZT* values reaching 0.5 at 800 K showing the potentiality of these unexplored materials for thermoelectricity. No investigation of the properties of SrCuP were reported to our knowledge. The copper-phosphide materials reported in the literature were synthesized by melting the constituting elements at high temperature [16,19]. Nevertheless, the use of phosphorus at high temperature can be dangerous and another synthesis method for SrCuP had to be developed.

In the present study, a new and safe synthesis method based on mechanical alloying is indeed successfully implemented for SrCuP. We also report the measurements of the thermoelectric properties in SrCuP and SrCuSb, for the first time to our knowledge in the case of SrCuP. These electronic and thermal transport properties results are discussed and compared to DFT calculations. The materials display high charge carriers mobilities and low thermal conductivities, making them as interesting for thermoelectricity.

2 Materials and Methods

2.1 Material synthesis

SrCuP was elaborated by mechanical alloying to avoid phosphorus manipulation in sealed tube. A stoichiometric Sr-Cu pre-alloy was prepared by melting in an induction furnace, Sr granules (Alfa Aesar, 99 %) and Cu rod (Alfa Aesar, 99.999 %) 5 times to ensure a good homogeneity. The surface of the obtained button was then filed in an Ar glovebox to limit the oxide formation. Then, the Sr-Cu pre-alloy was crushed in an agate mortar and inserted into a WC jar filled with P powder (Alfa Aesar, 100 mesh, red phosphorus, 98.9 %) in stoichiometric amount, and with 12 WC balls of 10 mm diameter, corresponding to a ball to powder ratio of 20. A Fritsch planetary micro mill Pulverisette 7 was used at a rotation speed of 600 rpm and for a milling duration of 5 h. The obtained powder was then annealed in glassy carbon crucible in silica tube sealed under Ar atmosphere (~ 0.2 bar) at 1073K for 3 days (heating ramp of 100 K/h). The aim of the annealing is to obtain micrometric crystallites with lower defect ratio than after mechanical alloying and to ensure the total reaction of phosphorus before sintering by SPS. A blueish powder was collected.

SrCuSb was prepared by heat treatment in silica tubes sealed under Ar (~0.2 bar). The starting materials, Sr granules (Alfa Aesar, 99 %), Cu powder (Alfa Aesar, 325 mesh, 99%) and Sb pieces (Chempur, 99.999%), were weighed in glovebox under Ar and placed in glassy carbon crucible with a 5 % excess of Sr. They were heated at 1223 K for 3 days applying temperature ramps of 100 K/h from room temperature to 773 K and 20 K/h up to 1223 K. A greenish compound was obtained.

Spark plasma sintering (SPS) of the annealed powders was performed using a Fuji 515S equipment of the “Plateforme Ile-de-France de Frittage”. Graphite molds lined with graphite paper (diameter of 10 mm) were used under Ar flow at 50 MPa and 1273 K for SrCuP and 75 MPa and 1073 K for SrCuSb. A pellet with a thickness of about 1.5 mm was prepared for SrCuP. In the case of SrCuSb, two pellets were prepared, one with a thickness of about 1.5 mm (for measurement of electrical properties perpendicular to the SPS pressing direction) and another one with a thickness of about 5.5 mm (for measurements along the SPS pressing direction). Densities of 98 % of the theoretical density were reached for both materials, as measured by the Archimedes method in isopropanol.

For transport properties measurements, disc-shaped samples with about 1 mm thickness were cut from the SPS pellets perpendicular to the pressing direction with a diamond saw and the face parallelism was corrected by polishing. With this cutting direction the thermal conductivities (λ) is measured along the SPS pressing direction and the electrical resistivities (ρ) is measured perpendicular to the SPS pressing direction. Bar-shaped samples of about 10 mm length and 1 mm thickness were then cut in the discs for measurement of Seebeck coefficients and Hall effect perpendicular to the SPS pression direction. In the case of SrCuSb, a parallelepipedal sample of about 5 mm length, 4 mm width and 0.8 mm thickness was cut along a thick pellet (thickness of 6 mm) for an additional measurement of ρ along the SPS pressing direction

2.2 Characterization

Powder X-ray diffraction (XRD) was carried out on a D8 Bruker diffractometer equipped with a graphite monochromator in the diffracted beam and using the Cu Kα radiation. A special airtight sample holder from Bruker was used to keep the powders under argon during the measurements. Rietveld refinements were made using the Fullprof program[20] . The chemical composition of the sintered pellets was analysed using a Zeiss Merlin Scanning Electron Microscopy (SEM) operating at 15 kV and equipped with an Energy-Dispersive X-ray (EDX) analyser from Oxford Instruments. The thermal stability was determined by simultaneous DTA / TGA measurements under argon flow at ambient pressure up to 1273 K and 1173 K for SrCuP and SrCuSb respectively, using a Setaram SETSYS Evolution 16 system. About 10 mg of powder were introduced in alumina crucibles with alumina cap and heating and cooling ramps of 10 K/min were applied.

High temperature electrical resistivity and Seebeck coefficient were measured from 300 K to 700 K under argon ($P\sim800$mbar) with a homemade apparatus[21]. The low temperature electrical resistivity and Hall effect measurements were carried out in a Physical Properties Measurement System (PPMS, Quantum Design) from 2.5 K to 300 K in AC mode and van der Pauw geometry. A magnetic field from -3 T to +3 T was ramped for Hall effect measurements. The thermal diffusivity, a, was measured by a laser flash method using a Netzsch LFA 427 system and the thermal conductivity

was derived from $\lambda = a \times C_p \times d$ with d the density and C_p, the heat capacity estimated at 74.83 J.mol^{-1}.K^{-1} from the Dulong and Petit's law. The electronic contribution (λ_e) to the thermal conductivity (λ) is derived from the well-known Wiedemann-Franz law, $\lambda_e = LT/\rho$, assuming $L = L_0 = 2.445 \times 10^{-8}$ V^2.K^{-2} as Lorenz number. The lattice contribution to the thermal conductivity (λ_{ph}) is obtained by subtracting λ_e to the measured thermal conductivity $\lambda_{ph} = \lambda - \lambda_e$. All these properties were measured during heating and cooling without any variation to check the stability of the materials during the measurements.

2.3 Calculations

DFT calculations were conducted using the projected augmented wave (PAW) method implemented in the Vienna *ab initio* Simulation Package (VASP) [22–25]. The exchange correlation was described by the generalized gradient approximation modified by Perdew, Burke, and Ernzerhof (GGA-PBE) [26] and also by the hybride HSE06 functional [27]. An energy cut-off of 600 eV was used for the plane wave basis set and a high-density *k*-points meshing was employed for integrations in the Brillouin zone of the BeZrSi structure type (21 × 21 × 10). These parameters ensured robust results in the total energy within convergence tolerance for the calculations set of 10^{-6} eV. We performed volume and ionic relaxation steps, and we considered collinear spin polarization. Blöchl correction was applied in a final step calculation[28].

Phonon dispersion bands were obtained by computing the atomic forces for different, finite atomic displacements [29] and a subsequent calculation and integration over the corresponding phonon frequencies, within the harmonic approximation. i.e. without any volume dependence, using the Phonopy code [30,31] . The phonon calculations were carried out within a 2 × 2 × 1 supercell with 3 atomic displacements for the BeZrSi structure-type.

3. Results and discussion

3.1 Synthesis, microstructure and thermal stability

The XRD patterns and Rietveld refinements of SrCuP and SrCuSb obtained after SPS are displayed in Fig. 1. The materials crystallize in the expected BeZrSi structure (space group $P6_3/mmc$), in agreement with the two previous reports of the literature [16,17] and this also confirms the calculated predictions [5]. As shown in Fig. 1-a, SrCuP is obtained for the first time by mechanical alloying. Nevertheless, some oxidation can be observed in the sintered material with the formation of $Sr_{10}(PO_4)_6O$ (4 at. %), $SrCu_4P_2$ (2 at.%) and $SrCu_2P_2$ (2 at.%). Most of these secondary phases are formed during annealing and SPS steps, as observed by comparison of XRD patterns of powders obtained directly after mechanical alloying and after SPS (see supporting information Fig. S1). The oxidation during post-treatments cannot be avoided due to the use of highly reactive phosphorus and strontium. Phosphorus-based materials are dangerous and difficult to handle, in particular at high-temperature in sealed tube. This new synthesis route involving mechanical alloying is therefore promising to make the synthesis of these materials easier. In SrCuP, we measure lattice parameters a = 4.146 Å and c = 8.382 Å in good agreement with the DFT calculated ones (a = 4.138 Å and c = 8.541 Å) and with the literature (a = 4.146 Å and c = 8.376 Å [16]).

In the case of SrCuSb, the material is obtained as a single phase in sealed tube with lattice parameters a = 4.527 Å and c = 8.752 Å. These values are also in good agreement with the calculated lattice parameters a = 4.547 Å and c = 8.926 Å and the reported ones (a = 4.52 Å and c = 8.81 Å [17]).

The narrow peaks observed by XRD indicate that the crystallite size is micrometric in both materials after annealing. It is confirmed by SEM observations (See supplementary information Fig. S2) made on annealed and sintered materials. Two sets of grains with sizes ~ 1 µm and ~ 10 µm can be observed in SrCuP with oxide phases at the grain boundaries whereas only grains sizes of more than 20 µm are observed in SrCuSb. Therefore, we do not expect grain size effect on the transport properties of the materials. The chemical compositions measured by EDS are close to the stoichiometry as shown in Table 1.

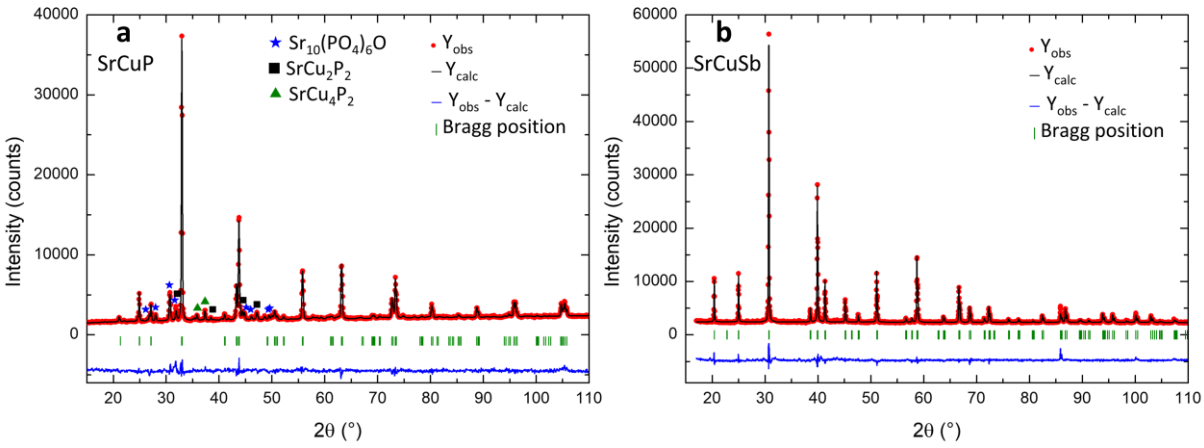

Fig. 1. XRD patterns and Rietveld refinement of *a*. SrCuP ($R_{wp} = 3.0\ \%, R_{\text{Bragg SrCuP}} = 2.6\ \%, R_{\text{Bragg } Sr_{10}(PO_4)_6O} = 16\ \%,$ $R_{\text{Bragg Sr}Cu_2P_2} = 8.5\ \%, R_{\text{Bragg Sr}Cu_4P_2} = 15\ \%$) and *b*. SrCuSb ($R_{wp} = 3.7\ \%, R_{\text{Bragg SrCuSb}} = 7.4\ \%$).

Table 1: Chemical composition (and standard deviation) of SrCuP and SrCuSb measured by EDS.

Composition	Sr (at. %)	Cu (at. %)	Sb (at. %)	P (at. %)
SrCuP	34.2 (0.2)	33.3 (0.5)	/	32.5 (0.3)
SrCuSb	32.8 (0.2)	33.0 (0.5)	34.2 (0.3)	/

The thermal stability of annealed SrCuP and SrCuSb (non-sintered powder) was studied by DTA / TGA under Ar flow (Fig. S3). Neither transformation nor weight change can be observed for both materials, showing their stability at least up to 1372K for SrCuP and 1173K for SrCuSb. This result is important regarding the sintering temperatures of the materials at 1273 K and 1073 K and the thermoelectric applications. Nonetheless, both compounds show fast oxidation in air, with surfaces of the sintered pellets quickly turning black in ambient conditions. Therefore, these materials must be stored under inert atmosphere.

3.2 Crystal structure and chemistry

The SrCu*X* (*X* = P or Sb) structure is displayed in Fig. 2. It can be described as planar Sr and hexagonal Cu*X* layers, stacked along the *c*-axis of the unit-cell. Along this axis, the Sr atoms align in columns

whereas the Cu and X atoms alternate, all at a distance *c*/2. Labelling the Sr layers “A”, the first Cu-*X* layer “B” and the next one “B’” leads to a stacking sequence … ABAB’A…

Table 2. Selected interatomic distances (in Å) found in SrCu*X*.

Compound	Sr – Sr // ***c***	Sr – Sr // (***a***, ***b***)	Sr – Cu(*X*)	Cu(*X*) – Cu(*X*)	Cu - *X*
SrCuP	4.191	4.146	3.181	4.146	2.394
SrCuSb	4.376	4.527	3.409	4.527	2.614

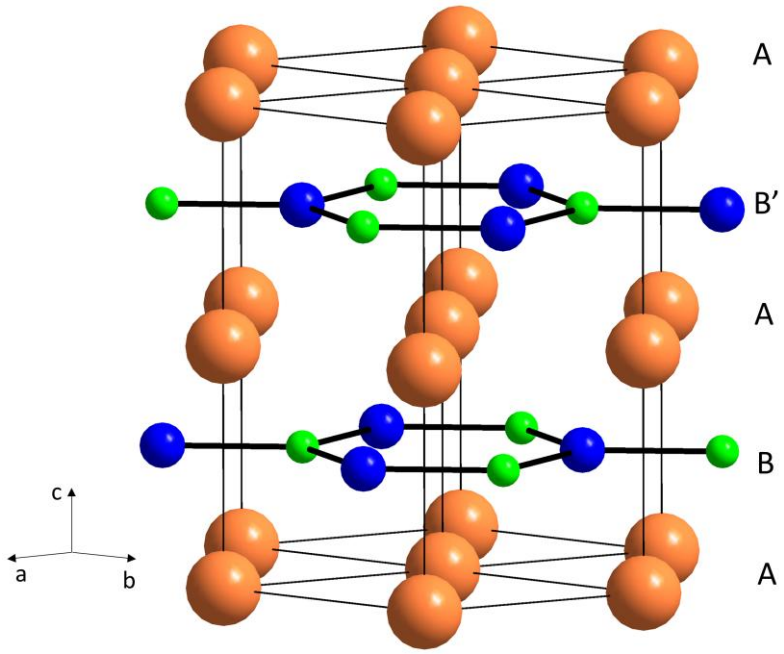

Fig. 2. SrCu*X* structure underlining the short Cu - *X* bonds (thick lines) and unit cell edges (thin lines). The orange spheres are Sr (*A* plane), the blue spheres are Cu and the green spheres are *X* (P, Sb) atoms (*B* and *B*’ planes).

The Sr – Sr distances exceed 4.1 Å (Table 2) as in other Sr-Cu and Sr-*X* binary compounds [32–36], whereas the Sr – Cu or the Sr – *X* distance is smaller than 3.4 Å. This strongly suggests that direct Sr – Sr bonds can be neglected and that the Sr atoms are rather bonded to the Cu and *X* atoms and are thus coordinated by 6 Cu and 6 *X* atoms forming a regular hexagon-based prism. In the Cu*X* plane, the Cu-Cu distance, and the *X* – *X* distances also exceed 4.1 Å whereas the Cu – *X* distance is short (2.4 – 2.6 Å), indicating that only covalent Cu – *X* bonds need to be considered. The Cu and *X* atoms

can thus be seen as forming a planar graphene-like hexagonal network with equivalent bonding role in the layer.

Given the electronegativity difference between Sr and the two other atoms (Sr: 0.95, Cu: 1.90; P: 2.19, Sb: 2.05, Pauling scale), one can surmise that SrCu*X* abides to the Zintl concepts: Sr gives away its two *5s* electrons to the Cu*X* sub-unit and the chemical formula can be written as $Sr^{2+}[CuX]^{2-}$. Assuming that the Cu *3d* states are full ($3d^{10}$) and do not take part in the bonding, the electronic configuration of the $[CuX]^{2-}$ complex can be written $2 \times (ns^2mp^2)$ with *n* and *m* = 3 or 4, depending on *X* = P or Sb. This is the electron configuration of two carbon atoms, which can form either a diamond network upon sp^3 hybridization or a graphene network upon sp^2 hybridization. The former hybridization would lead to a LiGaGe [37] or a $(LiTb)(CuP)_2$ [38] structure type whereas the latter leads to the effectively observed structure. In this scheme, the Cu(*X*) atoms are bound to *X*(Cu) atoms by 2-center σ- and π-bonds arising from sp^2 and p_z like orbitals, leaving no free electron pair. By analogy with graphene, large electronic mobility could be expected in the (*a*,*b*) plane. This Zintl "picture" of both compounds agrees well with the results of the DFT calculations. The projection on the elements of the DOS as presented in Fig. S4 and S5, indeed confirms that Cu *3d* states do not take part in the bonding since they correspond to the large peak found at -3 eV below the Fermi level E_F. The Fig. S4 is also consistent with the Zintl picture where Sr atom gives away its electron to Cu and P atoms: the former atom weakly contributes to the occupied states in the -1 eV – 0 eV energy range, compared to the latter atoms.

3.2 Calculated electronic structure

For SrCuP and SrCuSb, the calculated band structure and density of states (DOS) are presented in Fig.3. We observe a very small peak at E_F for both compounds. Even if the DOS are not exactly zero at E_F by using the PBE functional, we have shown in our screening method, explained in ref.[6], that

compounds which exhibit a low value in the DOS at E_F below 0.1 eV/states per atom can be considered as non-metallic, e.g. semi-metal or semi-conducting within the PBE approximation. This criterion has been empirically established by testing many chemical elements, binary and ternary transition metal compounds within the GGA scheme[6] . In agreement with their very small DOS at the Fermi level, no finite band gap can be noticed in both compounds.

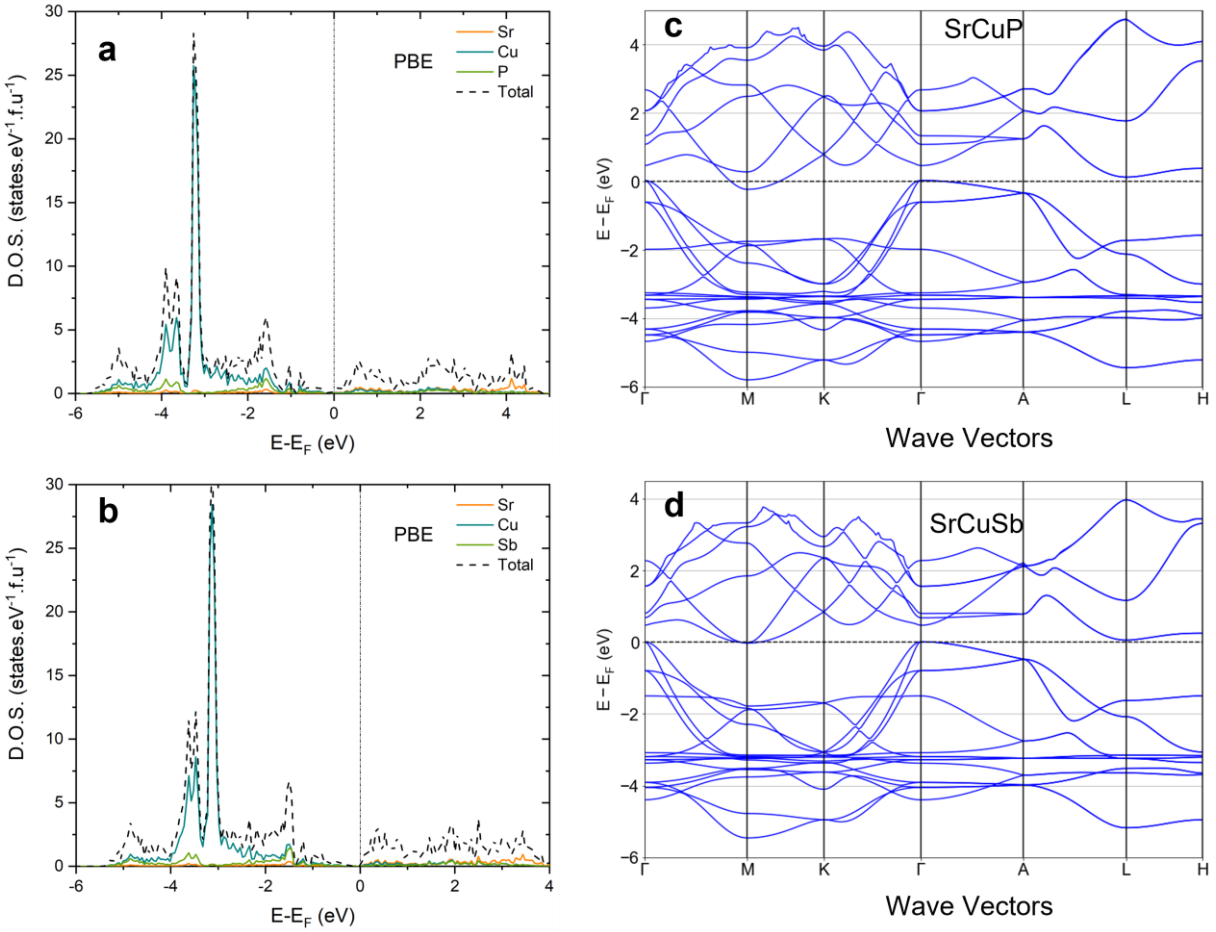

Fig. 3. Calculated total DOS and band structure for SrCuP (a and c) and SrCuSb (b and d). The Fermi energy E_F is chosen as origin of the energy.

A more detailed picture for both compounds can be drawn from the band structure (Fig. 3 *c* and *d*). On the one hand, the conduction band crosses E_F in SrCuP at the *M* direction and indirectly overlaps the valence bands over 0.3 eV at Γ point, leading to a semi-metallic ground state. On the other hand,

both the conduction and the valence bands indirectly contact each other at E_F in SrCuSb at *M* and Γ points, resulting in a zero-band gap semiconducting ground state. This band overlap and zero-band gap are too small to be firmly established within the GGA-PBE approximation in both compounds. It is hence difficult to conclude on the exact electronic nature of each compound. To go further, additional calculations with the hybrid functional (HSE06) have been performed on both compounds. On an enlarged energy scaled around E_F, the DOS comparison between both compounds and functional are presented in Fig. 4.

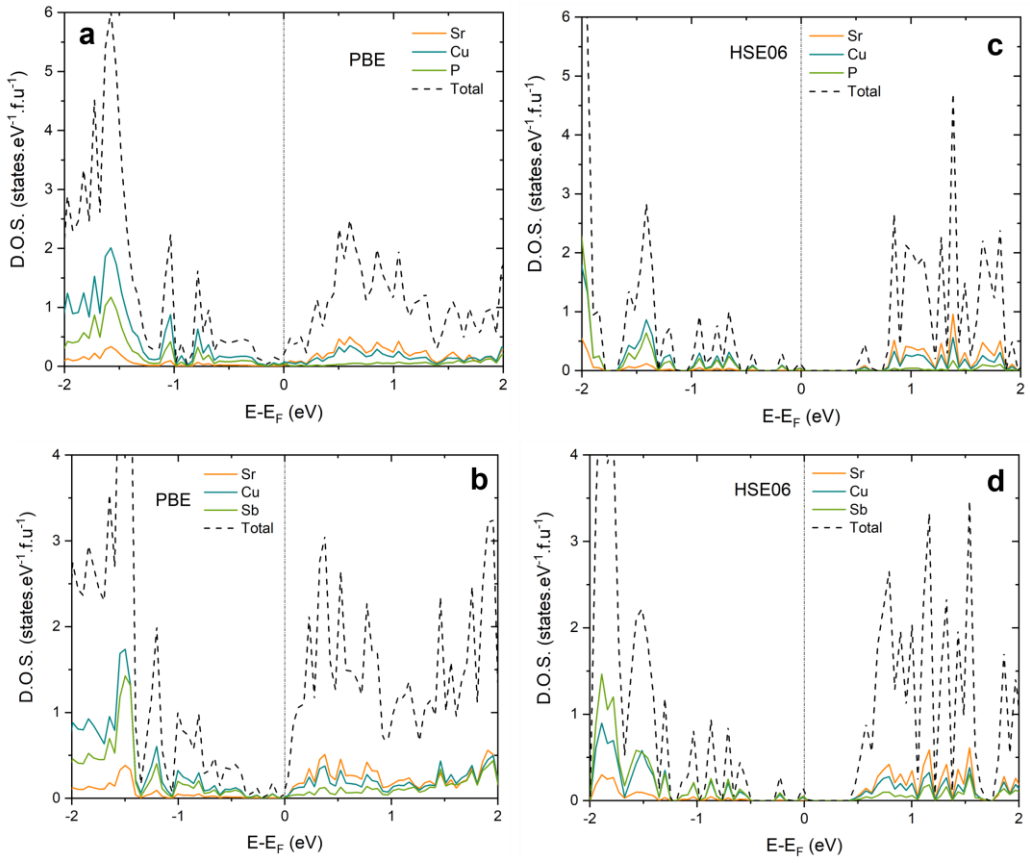

Fig. 4. Comparison between PBE and HSE06 functionals, calculated DOS for SrCuP (a and c) and SrCuSb (b and d)

Even though any clear band gap can be noticed with GGA-PBE calculations, HSE06 functionals clearly induced a relocation of the highest unoccupied bands leading to the apparition of a bandgap. Therefore, a band gap of 0.43 eV for SrCuP and 0.38 eV for SrCuSb can be derived with HSE06, confirming the semiconductor behavior of these materials. On the one hand, results from GGA-PBE

calculations stated that SrCuP and SrCuSb are either semi-metals or small-gap semiconductors; on the other hand, a clear band gap can be noticed with HSE06 functional. Regarding both results and considering that GGA-PBE are known to underestimate the energy gap, one can reasonably expect that both compounds present a small band gap and at least exhibit ground states favorable to good thermoelectric properties. This conclusion is strengthen by the indirect bandgap of 0.218 eV calculated in SrCuSb by Zheng *et al.* [18] within the PBE approximation coupled to the GW_0 approximation.

3.3 Experimental study of the thermoelectric properties

Measurements of electrical resistivity (ρ) and Seebeck coefficients (S) are reported in Fig. 5. Both SrCuP and SrCuSb show similar behaviors and the steady variations along the temperature ranges confirm that no structural transition occurs. The electrical resistivity of SrCuSb was measured on two samples along and perpendicular to the SPS pressing direction. These two measurements are very similar, showing that there is no texture or anisotropy effects on the electrical properties of SrCuSb and probably of SrCuP. The electrical resistivity of SrCuP and SrCuSb increases with raising temperature. That of SrCuP (1086 $\mu\Omega$.cm at room temperature) is much larger than that of SrCuSb (264 $\mu\Omega$.cm). Their Seebeck coefficient, S, is positive and increases linearly with raising temperature, starting from values of about 67 $\mu V.K^{-1}$ and 36 $\mu V.K^{-1}$ at 300 K respectively for SrCuP and SrCuSb.

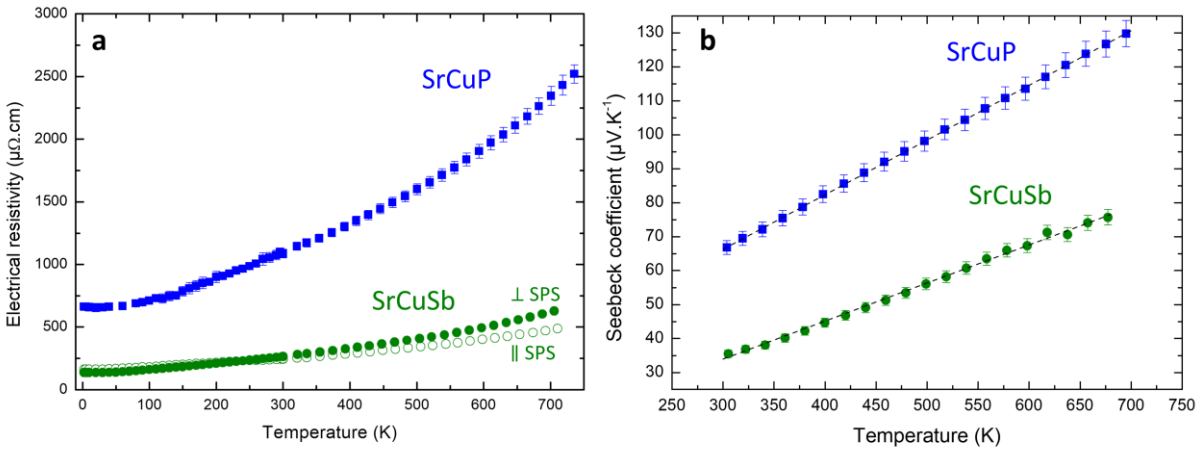

Fig. 5.a. Electrical resistivity of SrCuP and SrCuSb. The electrical resistivity of SrCuSb is measured on two samples along and perpendicular to the SPS pressing direction. b. Seebeck coefficient of SrCuP and SrCuSb. Dashed lines show linear fits used for the effective mass calculations.

To better understand the differences of electrical behaviors between SrCuP and SrCuSb, their hall coefficients (R_H) were measured perpendicular to the pressing direction (Fig. 6-a). Positive values were obtained, showing that both materials are *p*-type conductors with holes as major charge carriers, in agreement with their positive Seebeck coefficient. The R_H values are weakly temperature-dependent along the measured range, with slightly lower mean values for SrCuP ($R_H = 3.7 \times 10^{-8}$ m^3/c) than for SrCuSb ($R_H = 5.3 \times 10^{-8}$ m^3/c). This absence of variations with temperature is typical of semimetal or degenerate semiconductors. Within the hypothesis of electrical transport only by holes, we can estimate the charge carrier concentration, p, from $p = 1/(R_H e)$ (with e, the elementary charge). We find $p \approx 1.7 \times 10^{20}$ cm^{-3} for SrCuP and $p \approx 1.2 \times 10^{20}$ cm^{-3} for SrCuSb. These close results cannot explain the large differences of electrical resistivity between these two materials. The charge carrier mobility, μ, can be calculated by:

$$\mu = \frac{R_H}{\rho}$$

The results are given in Fig. 6-b. The mobility values are quite large in both materials, reaching 200 cm^2 V^{-1}.s^{-1} in SrCuSb at room temperature, which is interesting for the thermoelectric properties. It can be surmised that these large values could arise from the graphene-like structure of the Cu*X* layers. Nonetheless, we observe a lower mobility in SrCuP compared to SrCuSb. This explains that the larger electrical resistivity in SrCuP is due to a smaller mobility, which can most likely be ascribed to the occurrence of oxides as secondary phases (see part 3.1). This last compound would also certainly display a large value of mobility if it had been synthesized in purer form. We also observe that μ is nearly proportional to $T^{-0.7}$ in the case of SrCuP and $T^{-1/2}$ for SrCuSb at temperatures above 125 K. This suggests that additional scattering mechanisms probably occur in SrCuP, in agreement with its

smaller mobility. Again, these effects are most likely related to the formation of oxides as secondary phases at the annealing or sintering stage.

Overall, the results of the electrical properties measurements are in good agreement with the DFT calculations. Indeed, despite metal-like variations of the electrical resistivity with temperature, their large values are not typical of metals, but rather of degenerate semiconductors or of semimetals. Similar conclusions can be drawn from the charge carrier concentrations and the Seebeck coefficient values. Therefore, we cannot conclude on the exact electronic ground state of these compounds, but we can state that both are interesting for thermoelectricity. This experimentally confirms the validity of our screening procedure to single out thermoelectric compounds.

The charge carrier density of states effective mass can be estimated in metals or degenerate semiconductors from the slope of Seebeck coefficient variation with T given in Fig. 5-b using – within parabolic band and energy-independent scattering approximations – the following equation:

$$S = \frac{8\pi^2 k_B^2}{3eh^2} m^* \left(\frac{\pi}{3\mathrm{p}}\right)^{2/3} T$$

We find $m^* = 0.7\, m_e$ for SrCuP and $m^* = 0.4\, m_e$ for SrCuSb, in good agreement with [18] estimating $m^* = 0.47\, m_e$ in SrCuSb, with m_e the bare electron mass. These low effective masses are consistent with the values of mobilities found in both compounds.

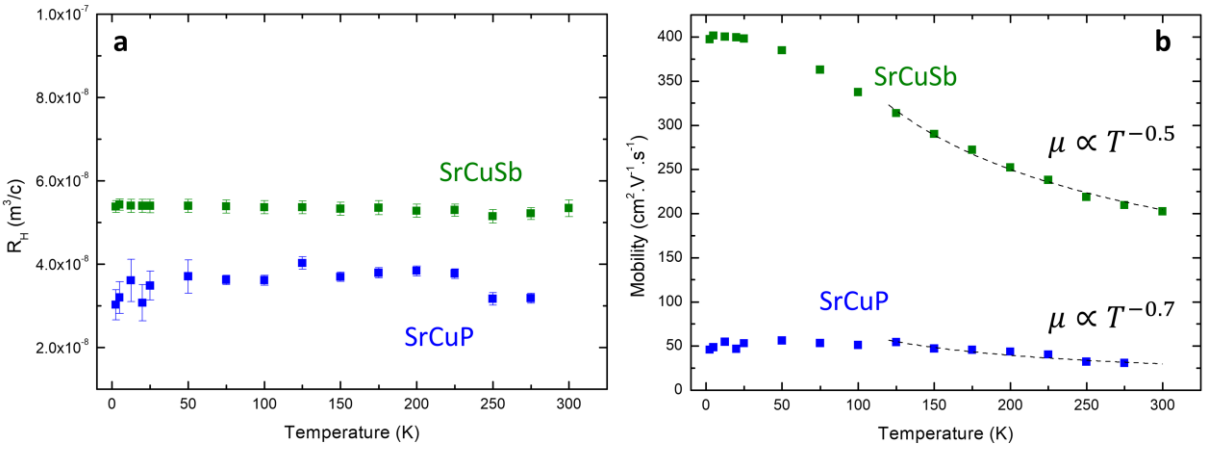

Fig. 6.a. Hall coefficient and b. charge carrier mobility of SrCuP and SrCuSb

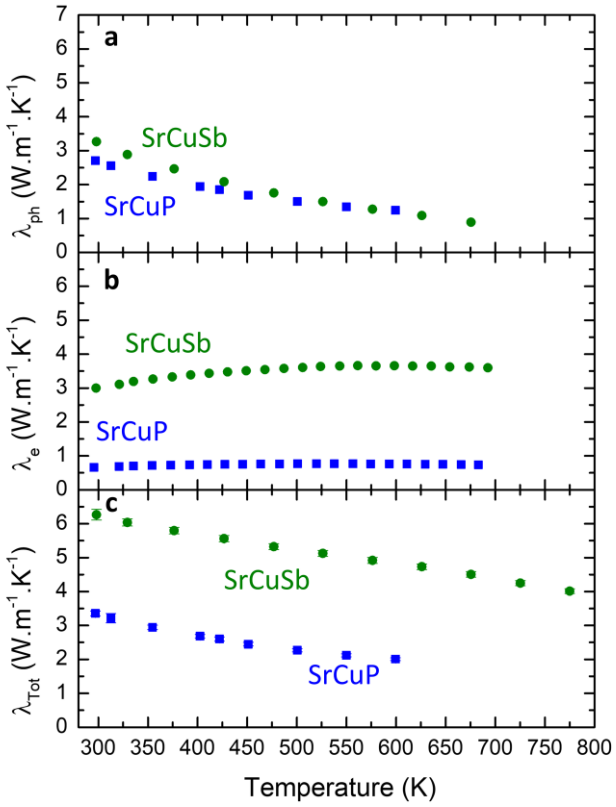

Fig. 7. a. Contributions of phonons and b. contributions of electrons to the thermal conductivity of SrCuP and SrCuSb. c. Total thermal conductivity.

The lattice thermal conductivity (λ_{ph}) and total thermal conductivity (λ) of SrCuP and SrCuSb are plotted versus temperature (300 – 800 K) in Fig. 7. We observe that λ_{ph} is smaller than 3.2 W m^{-1} K^{-1} in both compounds, a value remarkably low for such a simple structure but in good agreement with previous report of *Zheng et al.* [18] and the calculations of Zhou *et al.*[39] for SrCuSb . One paradigm is that to find a new thermoelectric material, a complex structure with many atoms per unit cells, leading to many non-heat-carrying optical phonon branches should be looked for. Obviously, compounds in the BeZrSi family do not abide by this concept and another explanation should be sought. The lattice dynamics of both compounds was hence calculated, and the phonon density of states (PDOS) is displayed in Fig. 8. In SrCuP (Fig. 8-a), a localized peak at 2.8 THz (11.6 meV or 134 K)

is mainly attributed to Sr contributions whereas the first peak in SrCuSb (Fig. 9b) is more spread from 1.8 to 2.2 THz, with mixed atomic vibrations. An analysis of the dispersion in the phonon bands can explain the difference. In SrCuP, the acoustic phonon branches are interrupted by narrow optical modes at 2.8 THz while in SrCuSb, similarly low-lying optical modes interrupt the acoustic branches around 1.8 THz up to 2.2 THz. In SrCuP, the narrow optical peak at 2.8 THz involves two modes at the Γ point in the Brillouin zone, corresponding to atomic displacements of Cu and P parallel to the (*a*, *b*) plane on the one side and Sr only displacements also parallel to (*a*, *b*) on the other side. For both modes, the displacements of the atoms are in phase in one plane and out of phase with the atoms of the next plane along the *c*-axis. In SrCuSb, this "Sr only" mode at Γ can also be found at 2.8 THz (Fig 8) well above the acoustic branches. The two modes at 1.8 and 2 THz at Γ involve Cu and Sb vibrations parallel to the (*a*, *b*) plane, while the mode at 2.2 THz involves vibrations of all three atoms parallel to the *c*-axis. Therefore, in both compounds, the acoustic branches that display the largest group velocity since they are the most dispersive, are interrupted by low energy optical modes, which limit the maximum energy that the former phonons can transport. Those results can be compared with a recent study of the origin of the low lattice thermal conductivity in the *X*CuSb (*X*=Ca, Sr and Ba) compounds [18]. In this paper, a complete investigation of BaCuSb, phonon dispersion combined with the study of the atomic displacement parameters, suggests that the low λ_{ph} should be attributed to the synergistic effects of both small group velocity and strong phonon scattering. Moreover, this situation is very reminiscent of the *A*Fe_4Sb_{12} skutterudites (*A* = Ba, Yb) that display lattice thermal conductivity values as small as 1.6 W m^{-1} K^{-1} at 300 K [40] and where low energy optical modes interrupt the acoustic branches[41–43]. In references [42,43], first principle calculations of the phonon – phonon scattering rate versus frequencies show that this quantity is increased in $BaFe_4Sb_{12}$ and $YbFe_4Sb_{12}$ over the entire phonon spectrum by these low energy optical phonons. By analogy of the calculated phonon spectra, it can be conjectured that a similar mechanism applies in the case of SrCu*X* (*X* = P, Sb), leading to the observed low lattice thermal conductivity values ($\sim$ 3 W m^{-1} K^{-1}) in both compounds.

However, another particularity can be noticed as both compounds display very similar values of lattice thermal conductivity, while the atomic mass of P is smaller than Sb. Based on similar values of resistivity parallel and perpendicular to the pressing axis upon sintering (Fig. 2), it can be here assumed that the polycrystalline texture is weak and plays a minor role in the other transport coefficients including the thermal conductivity, which remains weakly anisotropic. Two main other extrinsic reasons can contribute to this situation: (i) given the larger carrier concentration in SrCuP than in SrCuSb (Fig. 7), there is probably a larger amount of mass defects that will more often scatter the phonon in the former compound, leading to a reduced thermal conductivity; (ii) the influence on the thermal conductivity arising from secondary phases present in SrCuP cannot be discarded. More interestingly, an intrinsic mechanism can also be invoked to explain the low thermal conductivity in SrCuP. Focusing again on the low energy part of the spectrum, in SrCuP the optical peak at 2.8 THz in the PDOS (Fig. 8a) displays a full width at half maximum of less than 0.2 THz whereas it is more than 0.35 THz broad in SrCuSb. This arises from the nearly "flat band" character of these low energy optical modes in SrCuP (Fig. 8a) while the differing SrCuSb modes are more dispersive. According to ref. [43], the occurrence of a narrower peak in the PDOS of $YbFe_4Sb_{12}$ than in $BaFe_4Sb_{12}$ leads to a larger scattering probability across the phonon spectrum and drastically larger at the frequency and at twice the frequency of the low energy modes. Therefore, by analogy, the phonons would be more scattered by anharmonic phonon – phonon interaction in SrCuP than in SrCuSb, making its lattice thermal conductivity lower than expected. Of course, this scenario needs first-principles calculations of the lattice thermal conductivity to be confirmed. An anomalous mass-trend λ_{ph} has already been reported in this BeZrSi family [39] as for *X*CuSb (*X*= Ca, Sr and Ba), CaCuSb exhibits the smallest value of λ_{ph}. In this case, study shows that a lighter X atom bond more weakly with Cu-Sb rings, leading to a stronger vibrational anharmonicity.

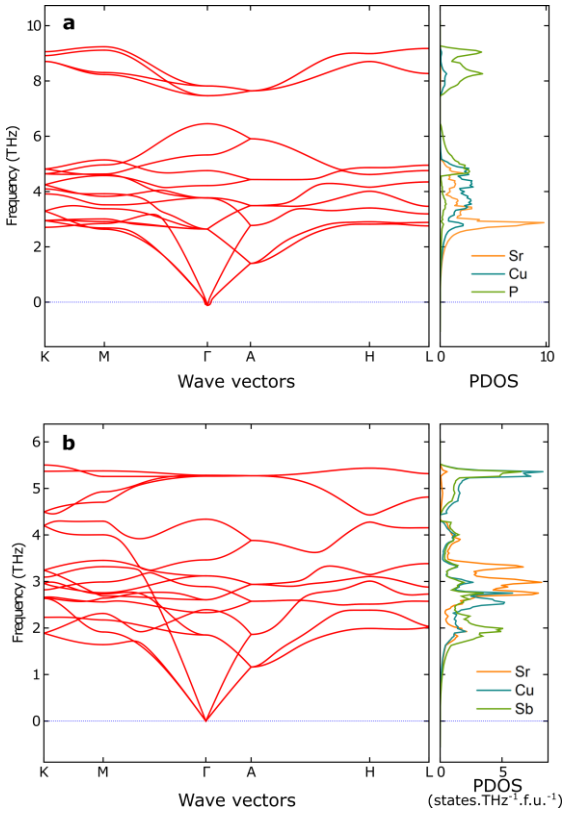

Fig. 8 a and b. Phonon dispersion and partial phonon densities of state of SrCuP and SrCuSb

The power factors, PF, and dimensionless figures of merit values, ZT, can be derived from the previous measurements by taking the following relations:

$$PF = \frac{S^2}{\rho}$$

$$ZT = \frac{S^2}{\rho\,\lambda}T$$

These quantities are plotted in Fig. 9. Despite smaller Seebeck coefficient, PF is higher in SrCuSb than in SrCuP because of the high electrical resistivity of SrCuP due to secondary phases as discussed previously. Maximum values of 7.0 and 9.7 $\mu W.cm^{-1}.K^{-2}$ are reached around 700 K for both SrCuP and SrCuSb respectively, confirming the high PF exceeding 10 $\mu W.cm^{-1}.K^{-2}$ at 1010 K reported by [18] in SrCuSb. These values are comparable to well-studied thermoelectric materials in the same temperature range such as PbTe [44], or SnTe [45,46]. These interesting results are explained by the high mobilities of charge carriers induced by the crystal structure. Moreover, the unusually low

thermal conductivities of the materials lead to ZT values of about 0.20 at 600 K and 0.14 at 650 K for SrCuP and SrCuSb respectively, without any intended doping. Additional improvement of PF and ZT could be expected by doping and reduction of thermal conductivity, making these materials promising for thermoelectricity.

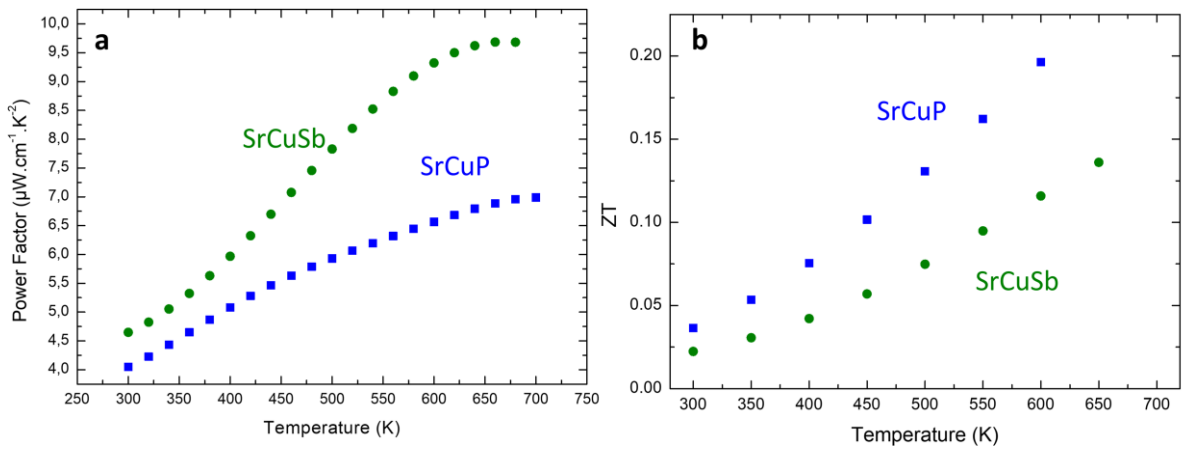

Fig. 9. a. Power factor and b. *ZT* values calculated for SrCuP and SrCuSb

Conclusions

The thermoelectric properties of SrCuP and SrCuSb were studied for the first time in the case of SrCuP. A new and safe synthesis method based on mechanical alloying was implemented for SrCuP. Both SrCu*X* (*X* = P or Sb) are *p*-type non-metallic compounds. The exact nature of their ground state, either semimetal or semiconducting (small gap), could not be determined from experiments and calculations. However, these ground states are both favorable for thermoelectric applications. The crystal structure, depicted within the Zintl concept, promotes the electrical transport with high charge carriers mobilities and low effective masses, related to graphene-like Cu*X* planes. Thus, maximal power factors of 7.0 and 9.7 $\mu W.cm^{-1}.K^{-2}$ are reached around 700 K. Rather low lattice thermal conductivities are found in these materials with such simple crystal structure. These results are explained by calculations of the vibrational properties in SrCu*X* showing that acoustic phonons are interrupted by low-energy optical branches. This favorable combination of good electronic

mobility and low thermal conductivity in SrCu*X* leads to thermoelectric figure of merit *ZT* = 0.20 (*X* = P) at 600 K and *ZT* = 0.14 (*X* = Sb) at 650 K.

Acknowledgments

The authors would like to thank the financial support of French ANR project ANR-18-CE05-0010. This study was made with the support of the Plateforme Ile-de-France de Frittage and Benjamin Villeroy for the sintering, Olivier Rouleau for the electrical properties measurements and Remy Pires for SEM. Calculations were performed using HPC resources from GENCI-CINES (No. A0060906175).

References

[1] D.M. Rowe, Thermoelectric Waste Heat Recovery as a Renewable Energy Source, 1 (2006) 11.
[2] H. Goldsmid, Bismuth Telluride and Its Alloys as Materials for Thermoelectric Generation, Materials. 7 (2014) 2577–2592. https://doi.org/10.3390/ma7042577.
[3] M.N. Tripathi, C.M. Bhandari, High-temperature thermoelectric performance of Si–Ge alloys, J. Phys.: Condens. Matter. 15 (2003) 5359–5370. https://doi.org/10.1088/0953-8984/15/31/303.
[4] Z.H. Dughaish, Lead telluride as a thermoelectric material for thermoelectric power generation, Physica B: Condensed Matter. 322 (2002) 205–223. https://doi.org/10.1016/S0921-4526(02)01187-0.
[5] C. Barreteau, J.-C. Crivello, J.-M. Joubert, E. Alleno, Looking for new thermoelectric materials among TMX intermetallics using high-throughput calculations, Computational Materials Science. 156 (2019) 96–103. https://doi.org/10.1016/j.commatsci.2018.09.030.
[6] C. Barreteau, J.-C. Crivello, J.-M. Joubert, E. Alleno, Optimization of Criteria for an Efficient Screening of New Thermoelectric Compounds: The TiNiSi Structure-Type as a Case-Study, ACS Comb. Sci. 22 (2020) 813–820. https://doi.org/10.1021/acscombsci.0c00133.
[7] P. Qiu, X. Huang, X. Chen, L. Chen, Enhanced thermoelectric performance by the combination of alloying and doping in TiCoSb-based half-Heusler compounds, Journal of Applied Physics. 106 (2009) 103703. https://doi.org/10.1063/1.3238363.
[8] S. Li, H. Zhu, J. Mao, Z. Feng, X. Li, C. Chen, F. Cao, X. Liu, D.J. Singh, Z. Ren, Q. Zhang, n-Type TaCoSn-Based Half-Heuslers as Promising Thermoelectric Materials, ACS Appl. Mater. Interfaces. 11 (2019) 41321–41329. https://doi.org/10.1021/acsami.9b13603.
[9] J.S. Young, R.G. Reddy, Processing and Thermoelectric Properties of TiNiSn Materials: A Review, J. of Materi Eng and Perform. 28 (2019) 5917–5930. https://doi.org/10.1007/s11665-019-04386-4.

[10] H. Zhu, J. Mao, Y. Li, J. Sun, Y. Wang, Q. Zhu, G. Li, Q. Song, J. Zhou, Y. Fu, R. He, T. Tong, Z. Liu, W. Ren, L. You, Z. Wang, J. Luo, A. Sotnikov, J. Bao, K. Nielsch, G. Chen, D.J. Singh, Z. Ren, Discovery of TaFeSb-based half-Heuslers with high thermoelectric performance, Nat Commun. 10 (2019) 270. https://doi.org/10.1038/s41467-018-08223-5.
[11] Y. Huang, H. Nagai, K. Hayashi, Y. Miyazaki, Preparation and thermoelectric properties of pseudogap intermetallic ($Ti_{1-x}V_x$)NiSi solid solutions, Journal of Alloys and Compounds. 771 (2019) 111–116. https://doi.org/10.1016/j.jallcom.2018.08.238.
[12] P. Gorai, A. Ganose, A. Faghaninia, A. Jain, V. Stevanović, Computational discovery of promising new n-type dopable ABX Zintl thermoelectric materials, Mater. Horiz. 7 (2020) 1809–1818. https://doi.org/10.1039/D0MH00197J.
[13] K. Peng, Z. Zhou, H. Wang, H. Wu, J. Ying, G. Han, X. Lu, G. Wang, X. Zhou, X. Chen, Exceptional Performance Driven by Planar Honeycomb Structure in a New High Temperature Thermoelectric Material BaAgAs, Advanced Functional Materials. 31 (2021) 2100583. https://doi.org/10.1002/adfm.202100583.
[14] S. Zheng, S. Xiao, K. Peng, Y. Pan, X. Yang, X. Lu, G. Han, B. Zhang, Z. Zhou, G. Wang, X. Zhou, Symmetry-Guaranteed High Carrier Mobility in Quasi-2D Thermoelectric Semiconductors, Advanced Materials. n/a (n.d.) 2210380. https://doi.org/10.1002/adma.202210380.
[15] Z. Zhou, K. Peng, S. Xiao, Y. Wei, Q. Dai, X. Lu, G. Wang, X. Zhou, Anomalous Thermoelectric Performance in Asymmetric Dirac Semimetal BaAgBi, J. Phys. Chem. Lett. 13 (2022) 2291–2298. https://doi.org/10.1021/acs.jpclett.2c00379.
[16] A. Mewis, ABX-Verbindungen mit Ni_2In-Struktur Darstellung und Struktur der Verbindungen CaCuP(As), SrCuP(As), SrAgP(As) und EuCuAs / ABX Compounds with the Structure Ni_2In Preparation and Crystal Structure of CaCuP(As), SrCuP(As), SrAgP(As), and EuCuAs, Zeitschrift für Naturforschung B. 33 (1978) 983–986. https://doi.org/10.1515/znb-1978-0906.
[17] B. Eisenmann, G. Cordier, H. Schäfer, CaCuSb(Bi) und SrCuSb(Bi) - Ternäre Phasen im „aufgefüllten“ NiAs-(Ni_2In)-Typ / CaCuSb(Bi) and SrCuSb(Bi) - Ternary Phases in the „Filled“ NiAs-(Ni_2In)-Structure, Zeitschrift für Naturforschung B. 29 (1974) 457–459. https://doi.org/10.1515/znb-1974-7-801.
[18] S. Zheng, K. Peng, S. Xiao, Z. Zhou, X. Lu, G. Han, B. Zhang, G. Wang, X. Zhou, Planar Zintl-phase high-temperature thermoelectric materials XCuSb (X = Ca, Sr, Ba) with low lattice thermal conductivity, J Adv Ceram. 11 (2022) 1604–1612. https://doi.org/10.1007/s40145-022-0634-y.
[19] R.J. Quinn, C. Stevens, H. Leong, A.D. Huxley, J.-W.G. Bos, New sustainable ternary copper phosphide thermoelectrics, Chem. Commun. 58 (2022) 11811–11814. https://doi.org/10.1039/D2CC03154J.
[20] J. Rodríguez-Carvajal, Recent advances in magnetic structure determination by neutron powder diffraction, Physica B: Condensed Matter. 192 (1993) 55–69. https://doi.org/10.1016/0921-4526(93)90108-I.
[21] O. Rouleau, E. Alleno, Measurement system of the Seebeck coefficient or of the electrical resistivity at high temperature, Review of Scientific Instruments. 84 (2013) 105103. https://doi.org/10.1063/1.4823527.
[22] G. Kresse, J. Hafner, *Ab initio* molecular dynamics for liquid metals, Phys. Rev. B. 47 (1993) 558–561. https://doi.org/10.1103/PhysRevB.47.558.

[23] G. Kresse, J. Furthmüller, Efficient iterative schemes for *ab initio* total-energy calculations using a plane-wave basis set, Phys. Rev. B. 54 (1996) 11169–11186. https://doi.org/10.1103/PhysRevB.54.11169.
[24] G. Kresse, D. Joubert, From ultrasoft pseudopotentials to the projector augmented-wave method, Phys. Rev. B. 59 (1999) 1758–1775. https://doi.org/10.1103/PhysRevB.59.1758.
[25] J. Hafner, G. Kresse, D. Vogtenhuber, M. Marsman, The Vienne Ab-Initio Simulation Package (VASP), (n.d.).
[26] J.P. Perdew, K. Burke, M. Ernzerhof, Generalized Gradient Approximation Made Simple, Phys. Rev. Lett. 77 (1996) 3865–3868. https://doi.org/10.1103/PhysRevLett.77.3865.
[27] L. Schimka, J. Harl, G. Kresse, Improved hybrid functional for solids: The HSEsol functional, J. Chem. Phys. 134 (2011) 024116. https://doi.org/10.1063/1.3524336.
[28] P.E. Blöchl, O. Jepsen, O.K. Andersen, Improved tetrahedron method for Brillouin-zone integrations, Phys. Rev. B. 49 (1994) 16223–16233. https://doi.org/10.1103/PhysRevB.49.16223.
[29] K. Parlinski, Z.Q. Li, Y. Kawazoe, First-Principles Determination of the Soft Mode in Cubic ZrO_2, Phys. Rev. Lett. 78 (1997) 4063–4066. https://doi.org/10.1103/PhysRevLett.78.4063.
[30] A. Togo, F. Oba, I. Tanaka, First-principles calculations of the ferroelastic transition between rutile-type and $CaCl_2$-type SiO_2 at high pressures, Phys. Rev. B. 78 (2008) 134106. https://doi.org/10.1103/PhysRevB.78.134106.
[31] A. Togo, I. Tanaka, First principles phonon calculations in materials science, Scripta Materialia. 108 (2015) 1–5. https://doi.org/10.1016/j.scriptamat.2015.07.021.
[32] G. Bruzzone, The binary systems calcium-copper, strontium-copper and barium-copper, Journal of the Less Common Metals. 25 (1971) 361–366. https://doi.org/10.1016/0022-5088(71)90178-0.
[33] J.-A. Dolyniuk, H. He, A.S. Ivanov, A.I. Boldyrev, S. Bobev, K. Kovnir, Ba and Sr Binary Phosphides: Synthesis, Crystal Structures, and Bonding Analysis, Inorg. Chem. 54 (2015) 8608–8616. https://doi.org/10.1021/acs.inorgchem.5b01253.
[34] H.-G. von Schnering, M. Wittmann, D. Sommer, Zur Chemie und Strukturchemie der Phosphide und Polyphosphide, Zeitschrift für anorganische und allgemeine Chemie. 510 (1984) 61–71. https://doi.org/10.1002/zaac.19845100310.
[35] K. Deller, B. Eisenmann, Notizen: $SrSb_2$, eine neue Zintlphase., Zeitschrift Für Naturforschung B. 31 (1976) 1146–1147. https://doi.org/10.1515/znb-1976-0829.
[36] A. Rehr, S.M. Kauzlarich, Sr<sub>11<\sub>Sb<sub>10<\sub>, Acta Cryst C. 50 (1994) 1859–1861. https://doi.org/10.1107/S0108270194003951.
[37] W. Bockelmann, H. Jacobs, H.-U. Schuster, Notizen: Die Kristallstruktur der Verbindung LiGaGe, Zeitschrift Für Naturforschung B. 25 (1970) 1305–1306. https://doi.org/10.1515/znb-1970-1120.
[38] A. Mahan, A. Mewis, AB_2X_2 -Verbindungen mit $CaAl_2Si_2$-Struktur, IX [1] / AB_2X_2 Compounds with the $CaAl_2Si_2$ Structure, IX [1], Zeitschrift Für Naturforschung B. 38 (1983) 1041–1045. https://doi.org/10.1515/znb-1983-0902.
[39] Z.Z. Zhou, K.L. Peng, H.X. Fu, H. Wu, G.Y. Wang, X.Y. Zhou, Abnormally Low Lattice Thermal Conductivity in ABX Honeycomb Compounds, Phys. Rev. Appl. 16 (2021) 064034. https://doi.org/10.1103/PhysRevApplied.16.064034.

[40] E. Matsuoka, K. Hayashi, A. Ikeda, K. Tanaka, T. Takabatake, M. Matsumura, Nearly Ferromagnetic Metals AFe_4Sb_{12} (A = Ca, Sr, and Ba), J. Phys. Soc. Jpn. 74 (2005) 1382–1385. https://doi.org/10.1143/JPSJ.74.1382.
[41] M.M. Koza, L. Capogna, A. Leithe-Jasper, H. Rosner, W. Schnelle, H. Mutka, M.R. Johnson, C. Ritter, Y. Grin, Vibrational dynamics of filled skutterudites $M_{1-x}Fe_4Sb_{12}$ (M=Ca, Sr, Ba, and Yb), Phys. Rev. B. 81 (2010) 174302. https://doi.org/10.1103/PhysRevB.81.174302.
[42] W. Li, N. Mingo, Thermal conductivity of fully filled skutterudites: Role of the filler, Phys. Rev. B. 89 (2014) 184304. https://doi.org/10.1103/PhysRevB.89.184304.
[43] W. Li, N. Mingo, Ultralow lattice thermal conductivity of the fully filled skutterudite YFe_4Sb_{12} due to the flat avoided-crossing filler modes, Phys. Rev. B. 91 (2015) 144304. https://doi.org/10.1103/PhysRevB.91.144304.
[44] B. Paul, A.K. V, P. Banerji, Embedded Ag-rich nanodots in PbTe: Enhancement of thermoelectric properties through energy filtering of the carriers, Journal of Applied Physics. 108 (2010) 064322. https://doi.org/10.1063/1.3488621.
[45] Y. Chen, M.D. Nielsen, Y.-B. Gao, T.-J. Zhu, X. Zhao, J.P. Heremans, SnTe-AgSbTe2 Thermoelectric Alloys, Adv. Energy Mater. 2 (2012) 58–62. https://doi.org/10.1002/aenm.201100460.
[46] S. Li, X. Li, Z. Ren, Q. Zhang, Recent progress towards high performance of tin chalcogenide thermoelectric materials, J. Mater. Chem. A. 6 (2018) 2432–2448. https://doi.org/10.1039/C7TA09941J.